Scalable Purification of Boron Nitride Nanotubes via Wet Thermal Etching

Daniel M. Marincel,[†,∇,=] Mohammed Adnan,[†,○,=] Junchi Ma,[†] E. Amram Bengio,[†] Mitchell A. Trafford,[†] Olga Kleinerman,[‡] Dmitry Kosynkin,[†] Sang-Hyon Chu,[∥] Cheol Park,[⊥] Samuel J.A. Hocker,[⊥] Catharine Fay,[⊥] Sivaram Arepalli,[#] Angel A. Martí,[§] Yeshayahu Talmon,[‡] and Matteo Pasquali[*,†,§,#]

[†] Department of Chemical and Biomolecular Engineering, The Smalley-Curl Institute, Rice University, 6100 Main Street, MS 369, Houston, Texas 77005, United States

[‡] Department of Chemical Engineering, Technion-Israel Institute of Technology and the Russell Berrie Nanotechnology Institute (RBNI), Haifa 3200003, Israel

[∥] National Institute of Aerospace, 100 Exploration Way, Hampton, Virginia 23666, United States

[⊥] Advanced Materials and Processing Branch, NASA Langley Research Center, Hampton, Virginia 23681, United States

[#] Department of Materials Science and NanoEngineering, Rice University, 6100 Main Street, Houston, Texas 77005, United States

[§] Department of Chemistry, The Smalley-Curl Institute, Rice University, 6100 Main Street, MS 369, Houston, Texas 77005, United States

ABSTRACT: Boron nitride nanotubes (BNNT) are poised to fill an electrically insulating, high temperature, high strength niche. Despite significant progress over the past two decades, BNNTs are not yet synthesized in high enough quantity and quality to permit their use in engineering applications. The next necessary step to make BNNTs accessible for research and applications is to improve the availability of high quality BNNTs. Here, we present a scalable bulk purification technique that yields high purity BNNTs. Bulk synthesized material is introduced to a wet oxygen environment at elevated temperatures to remove elemental boron and hexagonal boron nitride impurities with a final yield of purified BNNTs near 10 wt%. This process shows full removal of impurities, as observed by scanning electron microscopy, cryogenic transmission electron microscopy, and high-resolution transmission electron microscopy. X-ray photoelectron spectroscopy and infrared spectroscopy show minimal BNNT functionalization, while high-resolution transmission electron microscopy shows damage to large-diameter BNNTs.

INTRODUCTION

Boron nitride nanotubes (BNNTs) exhibit high tensile strength,[1] high band gap (~6 eV)[2] independent of chirality,[3] high thermal conductivity (~350 W/m·K),[4] high neutron absorption cross-section for ^{10}B,[5,6] and resistance to oxidation in air with experimental measurements of stability ranging from 750 °C[7] to 900 °C.[8] These characteristics have been exploited in polymer and metal composites to improve mechanical properties[9−12] and to shield satellites and astronauts from neutron radiation.[13,14] BNNTs also have potential to be used as dielectrics in nanoelectronics[15,16] and development for medical imaging.[17,18]

However, only applications that require small amounts or low purity BNNTs have been possible due to difficulties in synthesis, purification, and processing.[19] Chemical vapor deposition[20−24] and template-based growth techniques[25,26] produce BNNTs with few impurities, but are still limited to milligram quantities. Recent advances in production through laser synthesis at high temperatures and pressures (HTP)[27] and plasma techniques[28,29] greatly improved the BNNT quality and production rate to gram-scale quantities, but contain impurities such as hexagonal boron nitride (*h*-BN) and elemental boron.[27,28] These impurities limit the thermal conductivity and mechanical strength imparted by BNNTs when used in composites.[9,30−32] Impurities are also expected to prevent the formation of an all-BNNT liquid crystal phase, which is needed for wet fiber spinning.[33]

While techniques to remove elemental boron without damaging the BNNTs are known,[34] the chemical similarities between *h*-BN and BNNTs make selective removal of *h*-BN difficult. The reported purification methods rely on preferentially dispersing BNNTs over *h*-BN in a solvent followed by multiple centrifugation cycles.[18,35−41] These methods often require sonication to disperse the BNNTs, which has been shown to damage the BNNTs,[42] and are limited to batch processing with relatively low-yield even in the cases where sonication is not required.

In this study, we apply a similar approach as the one used to oxidize elemental boron at elevated temperatures[34] to purify the BNNTs synthesized by the HTP method.[27] Previous studies indicate that *h*-BN preferentially reacts along the edges rather than on the basal plane at 900 °C in dry air.[43] In both *h*-BN and BNNTs, local defects,[15,44−46] vacancies,[47−51] edges, dangling bonds,[46,52−54] and

dopants[55] increase the reactivity with neutral and charged reagents due to bond frustrations. We propose that *h*-BN particles in the as-synthesized material have a higher (hk0) surface-to-volume ratio than crystalline BNNTs, consequently having a greater number of frustrated bonds which will react at a lower temperature than BNNTs.

EXPERIMENTAL

Wet Thermal Processing Setup

Figure 1 shows a schematic of the setup used to purify raw BNNTs. Pure oxygen and/or nitrogen with controlled flow rate (using flow meters 1 and 2) flows into the tube furnace (7) via a source of hot water at 90 °C (6) while valve 3 remains open. A bypass valve (4) was used to provide an alternative path for dry oxygen or nitrogen to reach the tube furnace. The stainless-steel tube (6) between the water bubbler and furnace was heated using a heating tape at 90 °C to ensure no loss of steam due to condensation. An alumina crucible containing the sample (*h*-BN, precipitates, or raw BNNTs) was placed at the center of the tube furnace (7), which was plugged with refractory blocks on either end to minimize heat loss, for 24 h at the maximum processing temperature. The cooled effluent gas was filtered through water (9) and vented to atmosphere (10). An empty flask (8) prevented water from entering the furnace.

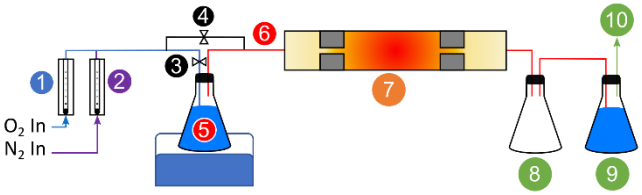

Figure 1. Schematic of the purification setup

Initial experiments on *h*-BN and precipitates of raw BNNTs obtained via density-driven separation in chlorosulfonic acid (CSA)[41] provided initial gas flow rates, times, and temperatures for analyzing as-produced BNNTs. Experiments on the reaction temperature and time were conducted using 50 mg of as-produced BNNTs. The purification process was assessed by the mass yield in weight percent (wt%), morphology, elemental analysis, and IR spectra of the unpurified and purified product. Details on purification of *h*-BN and precipitates are shown in the Supporting Information sections S1 and S2.

Scanning Electron Microscopy

The product from the reaction at different temperatures was transferred to carbon tape for scanning electron microscopy (SEM). Because BNNTs are insulating, a 5 nm thick layer of gold was sputtered (Denton Vacuum Desk V) onto the samples in order to avoid charging. Images were collected using an FEI Quanta 400 Scanning Electron Microscope with a 5 kV field, 2.0 nm spot size, and 3.0 mm working distance.

X-Ray Photoelectron Spectroscopy

X-ray photoelectron spectroscopy (XPS) was carried out using a Phi-Quantera spectrophotometer. Samples were freeze-dried under vacuum and annealed at 280 °C to remove adventitious carbon prior to characterization. X-rays from an aluminum source were used with 45.3 W power and a 200 μm spot size. Survey scans on the samples used an X-ray pass energy of 140 eV with a collection time of 80 ms per point with binding energies 1100 – 0 eV and a step-size of 0.5 eV. Elemental scans used an X-ray pass energy of 26 or 69 eV with a collection time of 200 ms per point and a step-size of 0.1 eV. Due to surface inhomogeneity in specimen thickness and overcharging in the samples, the peak positions for boron, nitrogen, and oxygen were shift-corrected to 190.7 eV for B1s peak, 398.2 eV for N1s peak, 533.3 eV for O1s peak, and 285.9 eV for C1s peak. Gaussian deconvolutions were performed using PHI Multipak, Version 9.5.0.8 on each spectrum and normalized to discern chemical compositions. This procedure minimizes contributions from specimen thickness and overcharging to permit direct comparison of spectra. All peak comparisons were done in reference to the Handbook of X-ray Photoelectron Spectroscopy[56] and the National Institute of Science and Technology X-ray Photoelectron Spectroscopy Database.[57] Details on the deconvolutions are provided in the Supporting Information section S3.

Thermogravimetric Analysis

Thermogravimetric analysis (TGA, TA Instruments Q-600) was conducted on raw BNNTs (5.6 mg) and the reaction products after wet thermal etching at 500 °C (3.7 mg), 675 °C (1.3 mg), 705 °C (0.9 mg), and 715 °C (0.4 mg). The temperature was ramped from 50 °C to 120 °C at 10 °C/min, held for 40 min to desorb moisture, then ramped to 1100 °C at 5 °C/min. Dry air was continually flowed across the samples at 100 ml/h while heating.

Infrared Spectroscopy

0.15 mg of solid sample was ground with 300 mg of KBr using a mortar and pestle. The samples were dried at 115 °C for 48 h then pressed into a disc. Solid samples were analyzed (Nicolet FTIR iS50-FT-IR) with a KBr beam splitter and detector. 128 scans from 400 – 4000 cm^{-1} with 4 cm^{-1} resolution were averaged, and then the background data was subtracted. The spectra were normalized to the *h*-BN longitudinal vibration mode at 1364 cm^{-1}.

Cryogenic Transmission Electron Microscopy

Cryo-TEM was performed with a Tecnai T12 G^2 electron microscope equipped with a LaB_6 electron gun and operated at an accelerating voltage of 120 kV. Specimens were first allowed to reach temperatures below −178 °C in a Gatan 626 (FEI) cryo-holder inside the microscope prior to imaging. Electron-beam radiation damage to nanotubes was minimized by examining the cryo-specimens using the low-dose imaging mode. Images were recorded digitally by a Gatan US1000 CCD camera, using the Digital Micrograph software.

High Resolution Transmission Electron Microscopy

Transmission electron microscopy (TEM) of the reaction products was conducted in order to qualitatively assess the presence of impurities and to determine damage incurred by the BNNTs through the purification process. To prepare thin films for TEM imaging, the reaction products were thinned by successive tearing between two pieces of tape. Once a sufficiently thin sample was obtained, tape residues were removed by rinsing with acetone and chloroform. The sample was then collected onto a copper grid. TEM was carried out using a JEOL 2100F field-emission TEM at an accelerating voltage of 200 kV. To reduce charging problems during TEM imaging, the largest spot size available was used for imaging in order to limit electron dose. A fine mesh size (> 2000) copper grid aided in charge dissipation due to the increased chance

that imageable parts of the sample would lie next to the electrically conducting grid.

RESULTS AND DISCUSSION

Reaction Mechanism

Scheme 1 describes the reactions involved in the wet thermal processing. At all temperatures explored in this report, elemental boron reacts with oxygen or steam to form boron oxide.[58,59] Metaboric acid ($(BOH)_3O_3$) is formed as boron oxide encounters water in the form of steam.[60] Exposure to excess steam reacts with metaboric acid to form gaseous boric acid ($B(OH)_3$). As boric acid gas is carried away as effluent, more surface is exposed for further reaction.

Scheme 1. Reactions involved in the wet thermal etching of boron and boron nitride polymorphs.

$$4B_{(s)} + 3O_{2(g)} \rightarrow 2B_2O_{3(s)}$$

$$4B_{(s)} + 6H_2O_{(g)} \rightarrow 2B_2O_{3(s)} + 6H_{2(g)}$$

$$3B_2O_{3(s)} + 3H_2O_{(g)} \rightarrow 2(BOH)_3O_{3(g)}$$

$$HBO_{2(g)} + H_2O_{(g)} \rightarrow B(OH)_{3(g)}$$

$$BN_{(s)} + 3H_2O_{(g)} \rightarrow B(OH)_{3(g)} + NH_{3(g)}$$

Similarly, at sufficiently high temperatures, BN particles with exposed defect sites react with oxygen to form boric acid and ammonia.[61] After boric acid removal, further high-energy surfaces are exposed for reaction. This continuous reaction between boron, BN, oxygen, and steam etches the high surface area particles. Similar to studies on carbon nanotube etching and purification,[62–64] we predict that the (hk0) edges of h-BN are most reactive due to a high concentration of dangling bonds;[43,46,52–54] we also expect higher reactivity of defect sites and ends of BNNTs, which may lead to BNNT shortening.

Mass Yield and SEM Analysis

The gray raw product synthesized by the HTP method turned completely white after undergoing the wet thermal etching at 500 °C as shown in Figure 2 with 70 wt% yield. SEM on the product shows that clusters of impurities remain after 500 °C etching (see Supporting Information section S4, Figure S8), indicating that not all impurities have been removed. Further removal of impurities was studied at reaction temperatures ranging from 675 °C to 730 °C.

The mass yield versus reaction temperature is illustrated in Figure 3. The initial yield of 25.3 wt% at 675 °C decreased to ~10 wt% for reaction temperatures of 700 °C to 710 °C. A yield of 5 wt% was obtained at 715 °C; the yield was below 2 wt% for higher reaction temperatures. It is likely that single walled and defective BNNTs are removed along with remaining *h*-BN and boron oxide at temperatures higher than 710 °C.

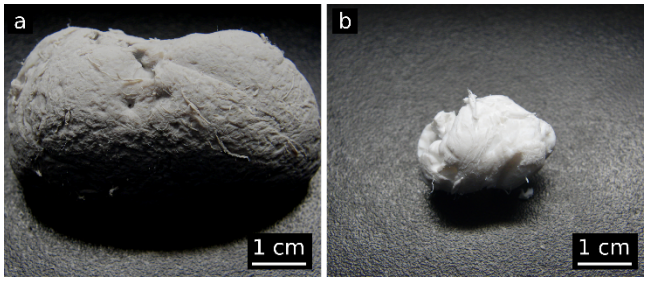

Figure 2. (a) As-received raw BNNTs. (b) Same raw BNNTs after wet thermal etching at 500 °C.

Although the degree of purification varies from the surface to the interior of the BNNT cluster, fewer impurity structures are visible by SEM with increasing reaction temperature as shown in Figure 3. Reactions at temperatures higher than 675 °C cause non-nanotube structures to be removed, with decreasing concentration of impurities as the temperature increases from 700 °C to 710 °C (Figure 3b). All non-fibril structures observable by SEM were removed from as-produced BNNTs at 715 °C and above (Figure 3c), leaving only a fibrous network of BNNTs.

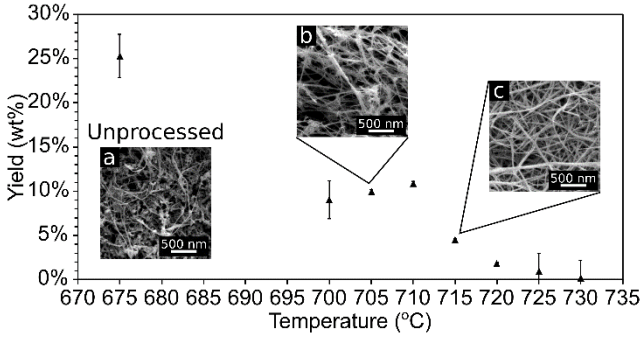

Figure 3. Mass yield in wt% of raw BNNTs undergoing wet thermal etching for 24 hours with oxygen flowing at 100 sccm. Error bars indicate error in the mass measurement. Error bars for 705 °C through 720 °C are smaller than the data point symbols. Insets: SEM images: (a) As-received raw BNNTs. Products remaining after wet thermal etching at (b) 705 °C and (c) 715 °C showing decreasing concentration of impurities.

X-Ray Photoelectron Spectroscopy

Survey scans on raw BNNTs and after wet thermal etching indicate the presence of boron, nitrogen, oxygen, and adventitious carbon (see Supporting Information section S5, Figure S9). The ratio of boron to nitrogen close to one indicates that the stoichiometry of the remaining material is unchanged after etching.[27] Quantitative values of the survey scans are tabulated in the Supporting Information section S3, Table S1.

Figure 4 shows binding energies between 188 – 195 eV, 395 – 402 eV, 530 – 538 eV, and 283 – 290 eV for B1s, N1s, O1s, and C1s respectively. Deconvolution of the as-synthesized material data shows peaks arising from elemental boron at ~187.3 eV,[65] B_6O at ~189.6 eV,[66] BN at ~190.6 eV,[67] $B_xN_yO_z$ at ~192.2 eV,[68] and B_2O_3 at ~193.4 eV.[69] A B1s peak due to elemental boron at 187.6 eV is distinctly visible using X-Rays with energy of 69 eV (see Supporting Information section S3, Figure S6).

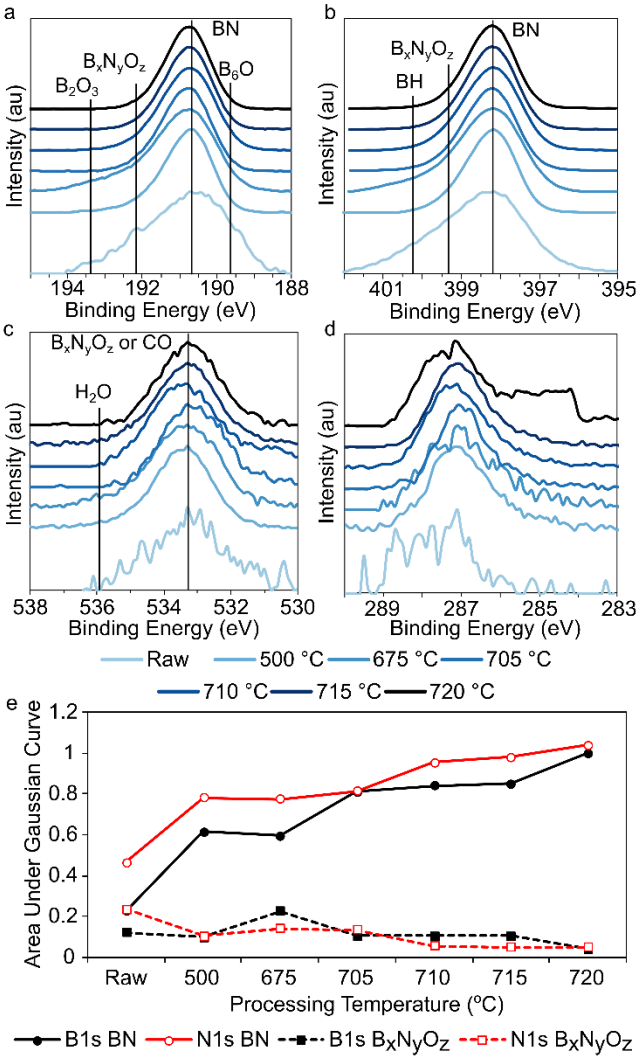

Figure 4. High resolution XPS spectra of BNNT products from processing at different temperatures for the (a) B1s, (b) N1s, (c) O1s, and (d) C1s peaks. (e) The area under the deconvoluted curves for the B1s and N1s peaks.

Processing at 500 °C removes elemental boron (see Supporting Information section S3). B_2O_3 forms due to the oxidation of elemental boron.[70] Although micrometer-sized boron particles have an oxidation onset near 600 °C,[71,72] it has previously been shown that nanoparticle boron reacts with oxygen below 500 °C and hydrolyzes with steam at even lower temperatures.[58,59] The B_2O_3 species observed via XPS are anticipated to remain due to kinetic limitations to volatilization.

Given the small concentration of oxygen measured in the survey scans (≤4%) and the minor contribution made by oxygen in the B1s and N1s elemental scans, there is only limited information that can be gained from the weak signal in the O1s elemental scan. Additionally, overlap of the $B_xN_yO_z$ and CO peak positions prevent direct determination of the amount of oxygen bonded to BN species. Instead, deconvolution for the B and N1s peaks was used to determine whether elemental boron or BN species react to form B_xO_y and $B_xN_yO_z$, respectively. The results are summarized in Figure 4e. Evidently, the proportion of BN species generally increases with processing temperature while the proportion of $B_xN_yO_z$ species decreases. An increase in proportion of $B_xN_yO_z$ species at 675 °C occurs due to reaction of highly defective *h*-BN species with oxygen. The concentration of $B_xN_yO_z$ species stays approximately constant for temperatures between 705 °C and 715 °C, corroborating the similar changes in mass observed in Figure 3. A significant drop in concentration of $B_xN_yO_z$ species is observed after processing at 720 °C. It should be noted that peaks obtained from the 720 °C process show high symmetry, indicating highly uniform atomic bonds.

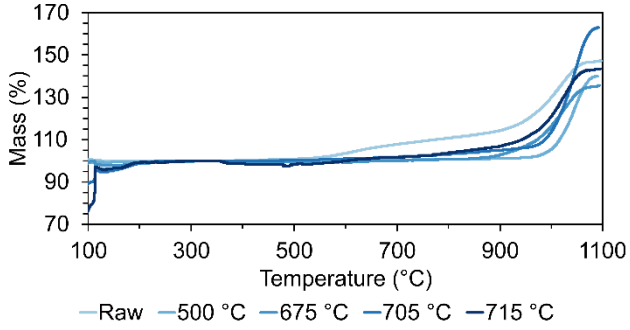

Figure 5. TGA of raw BNNTs and reaction products from wet thermal processing at 500 °C, 675 °C, 705 °C, and 715 °C.

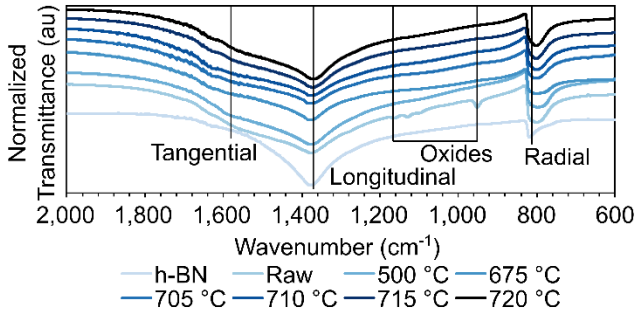

Figure 6. Transmission IR spectra for *h*-BN, raw BNNTs, and reaction products from wet thermal etching at 500 °C, 675 °C, 705 °C, 710 °C, 715 °C, 720 °C.

Thermogravimetric Analysis

TGA was used to assess the removal of boron and potential changes to the stability of the BN polymorphs after wet thermal processing. Data collected between 100 °C and 1100 °C for raw BNNTs and after processing at 500 °C, 675 °C, 705 °C, and 715 °C are presented in Figure 5.

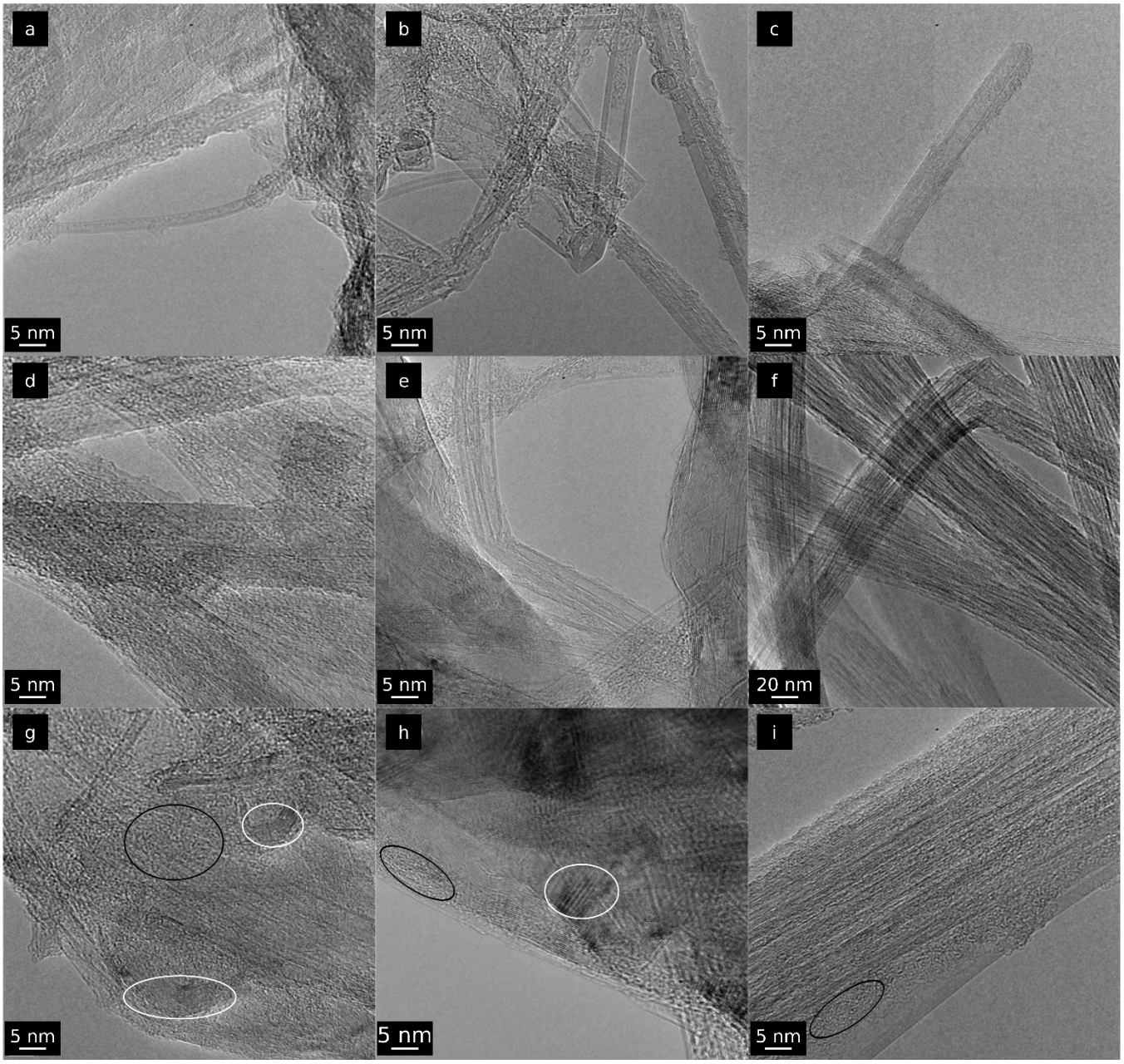

Figure 7. TEM micrographs of BNNTs after wet thermal etching showing (a, b, c) individual BNNTs, (d, e, f) aggregated BNNTs, and (g, h, i) primary impurities observed for each sample, including amorphous BN (black circles) and layered *h*-BN (white circles). (a, d, g) show the sample after purification at 500 °C, (b, e, h) at 675 °C, and (c, f, i) at 715 °C.

Mass gain between 500 and 700 °C is only observed for raw BNNTs and not after wet thermal processing. Since the onset of oxidation for boron is expected to be near 500 °C,[8] this indicates that all boron has been removed after wet thermal processing at 500 °C. All samples show a mass gain between 950 and 1000 °C of approximately 35 to 40%.

Infrared Spectroscopy

The spectra measured from transmission infrared spectroscopy are shown in Figure 6. The spectrum for *h*-BN shows only two major peaks belonging to an in-plane longitudinal vibration (L) of BN bonds at 1377 cm^{-1} and an out-of-plane vibration (R) at 815 cm^{-1}.[73] An additional peak near ~1540 cm^{-1} is observed for all BNNT samples. Previous reports in the BNNT literature argue that this peak is due to an in-plane tangential vibration (T) of BN bonds along the circumference of BNNTs and is an identifying fingerprint for BNNTs.[30,74] However, calculations[75,76] and experiments[73] indicate a peak for *h*-BN at ~1540 cm^{-1}. In the current work, analysis of this peak is further complicated by the presence of an ~2 a.u. shoulder at ~1620 cm^{-1} that is considered an artifact also seen in a blank KBr disk (see Supporting Information section S6, Figure S10).

The sharp absorption peaks at ~970 cm^{-1}, ~1130 cm^{-1}, and ~1170 cm^{-1} observed for as-synthesized BNNTs are attributed to the presence of small amounts of boron oxide, boric acid, or metaboric acid, formed when boron reacts with ambient oxygen and water after synthesis.

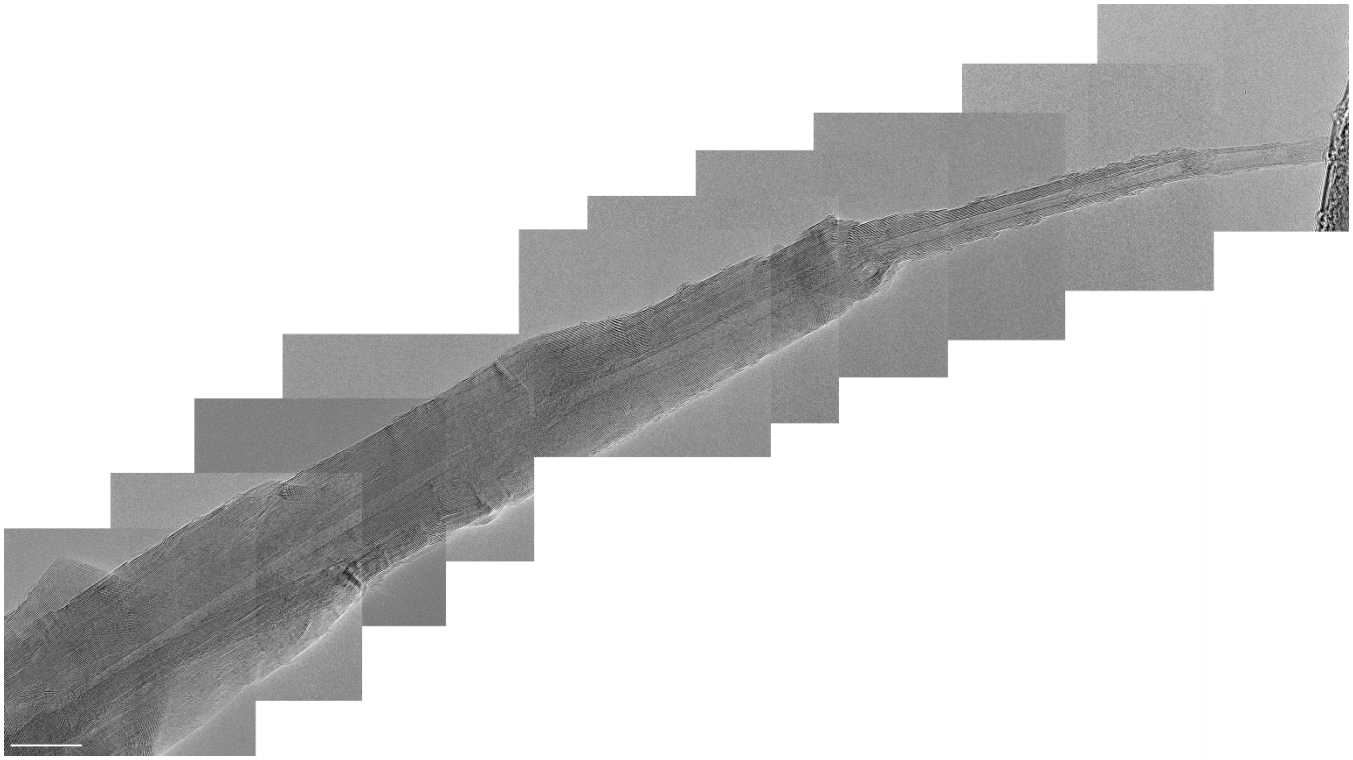

Figure 8. Montage of TEM micrographs showing a BNNT from the sample processed at 675 °C sample. Scale bar is 20 nm.

These identified oxide peaks are not present for the processed samples, reinforcing the observation that unbound boron oxide species are removed during processing. A broad shoulder centered near 1100 cm^{-1} develops for all samples that undergo thermal processing (including *h*-BN). To explain this broad shoulder, we consider that boron oxynitrides have vibrational modes within the same range as the soulder.[77] This shoulder does not decrease significantly until 715 °C, indicating the possibility of BN surface oxide functionalization and that the impurities observed by SEM after processing at 705 °C and 710 °C may be composed of boron oxynitrides.

TEM Analysis

Figure 7 shows typical TEM micrographs of the BNNT reaction products at different wet etching temperatures. As evidenced by Figure 7 (a-c), individual BNNTs can be observed in all samples. A wide range of BNNT diameters is observed, from only a few nm to almost 50 nm (see Figure 8). However, due to the presence of impurities and BNNT bundling, the observation of fully individualized BNNTs was a rare occurrence. The infrequent observation made obtaining a statistically significant BNNT diameter distribution considerably time-prohibitive.

Nevertheless, qualitative observations based on the micrographs of Figure 7 may still be helpful in guiding process optimization. For instance, comparison between Figure 7d and Figure 7f shows that, qualitatively, the BNNT bundles become cleaner as the purification temperature is increased. The presence of amorphous BN material on the BNNT walls (also shown at the highest temperature in Figure 7i) hinders the van der Waals interactions between individual BNNTs and therefore the formation of aligned fibrils, as observed previously in carbon nanotubes (CNTs).[33]

Comparison between Figure 7g and Figure 7h shows the relative importance of the various types of impurities present in the BNNT samples. In Figure 7g, large quantities of amorphous BN cover most of the sample's surface, and some layered *h*-BN structures are visible. In Figure 7h, however, these layered *h*-BN impurities seem to be the dominant type of impurity present in the sample. This is consistent with the results from XPS and TGA above. In Figure 7i, the only type of impurity visible is a thin layer of amorphous BN localized on the BNNT walls. We suspect that this is the most challenging type of impurity to remove without inducing oxidative damage to the BNNT walls.

Figure 8 shows a montage of ten TEM micrographs displaying a multi-walled BNNT from the 675 °C sample over a length of a few hundred nm. The montage shows how the nanotube's walls are progressively eliminated over the observed length of the tube. This is likely due to oxidative damage to the BNNT walls, but it is possible that this feature could also be a by-product of an imperfect BNNT synthesis reaction.

Cryo-TEM Analysis

Impurities left after purification were imaged using cryo-TEM with a large field of view to assess the relative concentration of impurities to nanotubes. While preparing cryo-TEM grids, purified BNNTs exhibited improved dissolution in CSA than raw BNNTs. BNNTs processed at 675 °C dispersed in CSA are shown in Figure 9a (white arrow). The contrast formation mechanism of BNNTs in CSA is similar to that of CNTs in CSA.[78] Black spots (black arrow) have a different morphology from the BNNTs,

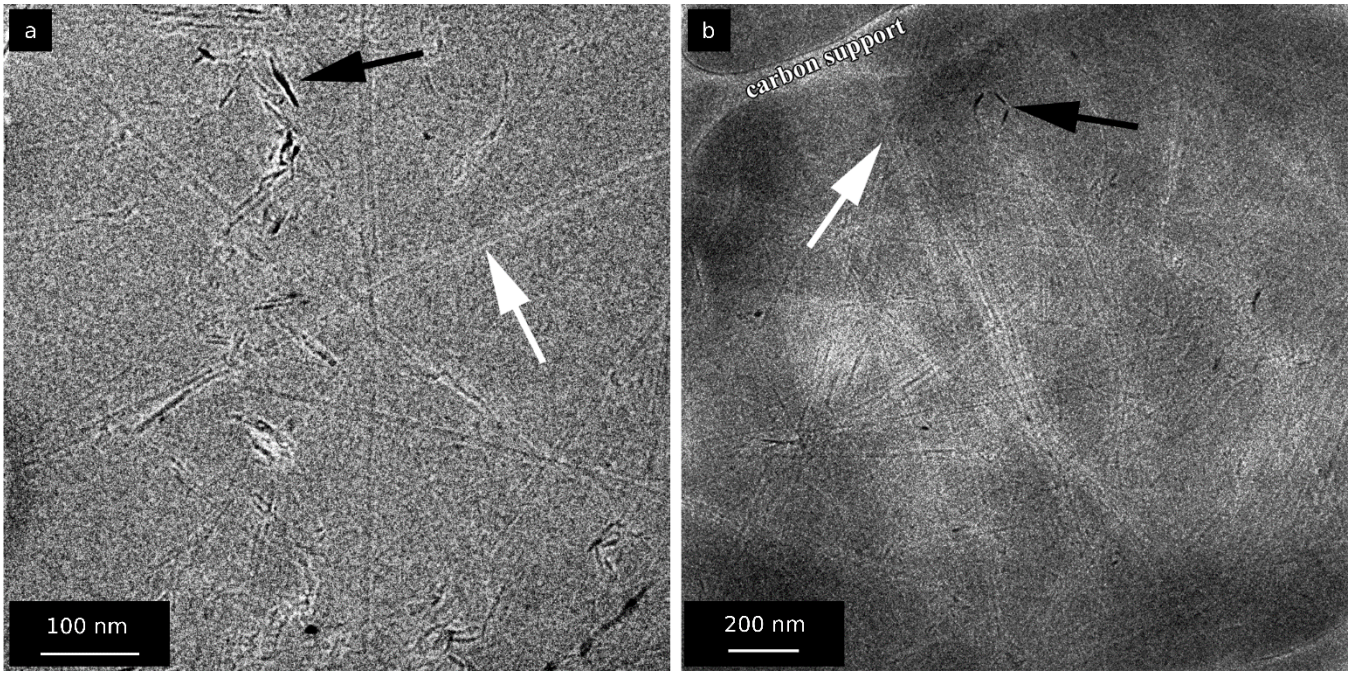

Figure 9. Cryo-TEM micrographs of BNNT products dissolved in CSA after processing at (a) 675 °C and (b) 715 °C. Black arrows point to byproducts formed during synthesis that are dispersed in CSA. The white arrows point to BNNTs.

indicating synthesis byproducts, while the contrast along the CSA/BNNT interface is enhanced due to CSA depletion during cryo-specimen exposure to the e-beam.[78] Most of the observed BNNTs are filled with acid, indicating wall damage or opened ends, as has been previously observed for CNTs[79] and BNNTs.[80] Additionally, *h*-BN aggregates are visible, similar to those observed when raw BNNTs are dispersed in CSA.[80]

Figure 9b shows BNNT processed at 715 °C dispersed in CSA (white arrow). Nanotubes have a denser packing after treatment at the higher temperature, with fewer non-nanotube particles observed inside the BNNT network (black arrow), indicating better BNNT dissolution in CSA. The difference in observed impurities between 675 °C and 715 °C corroborates the FTIR data, which indicated that *h*-BN non-nanotube compounds are removed above 710 °C. BNNT dissolution after processing at 715 °C is indicative of their pristine nature, similar to findings reported for as-synthesized BNNTs.[80]

CONCLUSIONS

BNNTs synthesized in gram-scale quantities contain considerable amounts of non-nanotube particles which can negatively impact properties when used in composite applications. These impurities consist of boron and *h*-BN particles formed as by-products during synthesis. The wet thermal etching technique developed in this work exploits the presence of higher number of highly defective surfaces to preferentially remove *h*-BN at lower temperatures than BNNTs. While SEM, cryo-TEM, XPS, and IR spectroscopy indicate that impurities are preferentially removed over BNNTs, HR-TEM indicates that BNNTs with defect sites are susceptible to damage. A maximum yield of ~10 wt% of pure BNNTs was obtained using our experimental setup at a relatively low temperature of 715 °C. It may be possible to further optimize reactor and reaction conditions to increase the yield of pure BNNTs. This method can be scaled up to purify gram-level BNNT quantities continuously if used as a purification unit subsequent to BNNT synthesis.

ASSOCIATED CONTENT

Supporting Information. The Supporting Information is available free of charge via the Internet at http://pubs.acs.org. Wet thermal processing of *h*-BN; wet thermal processing of raw BNNT precipitates; x-ray photoelectron spectroscopy; SEM of BNNT oxidation product; XPS survey scans of as-produced and processed BNNTs; FTIR.

AUTHOR INFORMATION

Corresponding Author

* Corresponding author: mp@rice.edu

Present Address

∇ D.M.M.: Department of Physics and Optical Engineering, Rose-Hulman Institute of Technology, 5500 Wabash Avenue, Terre Haute, Indiana 47803, United States.

° M.A.: Abu Dhabi Financial Group. Al Bateen Towers, C2 Tower, 14th Floor. PO Box: 112230, Abu Dhabi, UAE.

Author Contributions

=D.M.M. and M.A. contributed equally. D.M.M., M.A., and M.P., designed and conducted the experiments, analyzed data, and wrote the manuscript. J.M. conducted the wet thermal processing experiments. O.K. and Y.T. conducted and analyzed the cryo-EM experiments. E.A.B. and M.A.T. conducted and analyzed the TEM experiments. C.P., S.A., D.K. and A.A.M. assisted in analyzing the data and editing the manuscript. All authors discussed the results and implications at all stages and edited the manuscript.

Funding

Funding was provided by NASA grant NNX15AK72G, AFOSR grants FA9550-18-1-0014 and FA9550-15-1-0370, NSF CHE 1610175, NSF CHE 1807737 and the United States-Israel Binational Science Foundation grants 2012223 and 2016161. D.M.M. was

partially supported by a Wiess Teacher-Scholar Fellowship; M.A. was partially supported by a Ph.D. scholarship from Abu Dhabi National Oil Company (ADNOC). M.A.T. was supported by the NSF DGE# 1450681.

Notes

The authors declare no competing financial interests.

ACKNOWLEDGMENTS

BNNTs were provided by NASA Langley Research Center. Cryo-TEM and HR-SEM imaging was performed at the Laboratory for Electron Microscopy of Soft Matter, supported by the Technion Russell Berrie Nanotechnology Institute (RBNI).

ABBREVIATIONS

BNNT, boron nitride nanotube; HTP, high temperature and pressure; *h*-BN, hexagonal boron nitride; HBO_2, metaboric acid; H_3BO_3, boric acid; SEM, scanning electron microscopy; XPS, x-ray photoelectron spectroscopy; TGA, thermogravimetric analysis; FTIR, Fourier transform infrared spectroscopy; TEM, transmission electron microscopy; Cryo-TEM, cryogenic transmission electron microscopy; CSA, chlorosulfonic acid; BN, boron nitride; CNT, carbon nanotube.

REFERENCES

(1) Wang, J.; Lee, C. H.; Yap, Y. K. Recent Advancements in Boron Nitride Nanotubes. *Nanoscale* **2010**, *2* (10), 2028. https://doi.org/10.1039/c0nr00335b.

(2) Terauchi, M.; Tanaka, M.; Matsumoto, T.; Saito, Y. Electron Energy-Loss Spectroscopy Study of the Electronic Structure of Boron Nitride Nanotubes. *Microscopy* **1998**, *47* (4), 319–324. https://doi.org/10.1093/oxfordjournals.jmicro.a023598.

(3) Rubio, A.; Corkill, J. L.; Cohen, M. L. Theory of Graphitic Boron Nitride Nanotubes. *Phys. Rev. B* **1994**, *49* (7), 5081–5084. https://doi.org/10.1103/PhysRevB.49.5081.

(4) Chang, C. W.; Fennimore, A. M.; Afanasiev, A.; Okawa, D.; Ikuno, T.; Garcia, H.; Li, D.; Majumdar, A.; Zettl, A. Isotope Effect on the Thermal Conductivity of Boron Nitride Nanotubes. *Phys. Rev. Lett.* **2006**, *97* (8). https://doi.org/10.1103/PhysRevLett.97.085901.

(5) Tiano, A. L.; Park, C.; Lee, J. W.; Luong, H. H.; Gibbons, L. J.; Chu, S.-H.; Applin, S.; Gnoffo, P.; Lowther, S.; Kim, H. J.; et al. Boron Nitride Nanotube: Synthesis and Applications; Varadan, V. K., Ed.; San Diego, California, USA, 2014; p 906006. https://doi.org/10.1117/12.2045396.

(6) Ahmad, P.; Khandaker, M. U.; Amin, Y. M.; Khan, G.; Ramay, S. M.; Mahmood, A.; Amin, M.; Muhammad, N. Catalytic Growth of Vertically Aligned Neutron Sensitive 10boron Nitride Nanotubes. *J. Nanoparticle Res.* **2016**, *18* (1). https://doi.org/10.1007/s11051-016-3326-0.

(7) Nautiyal, P.; Loganathan, A.; Agrawal, R.; Boesl, B.; Wang, C.; Agarwal, A. Oxidative Unzipping and Transformation of High Aspect Ratio Boron Nitride Nanotubes into "White Graphene Oxide" Platelets. *Sci. Rep.* **2016**, *6* (1). https://doi.org/10.1038/srep29498.

(8) Chen, X.; Dmuchowski, C. M.; Park, C.; Fay, C. C.; Ke, C. Quantitative Characterization of Structural and Mechanical Properties of Boron Nitride Nanotubes in High Temperature Environments. *Sci. Rep.* **2017**, *7* (1). https://doi.org/10.1038/s41598-017-11795-9.

(9) Terao, T.; Zhi, C.; Bando, Y.; Mitome, M.; Tang, C.; Golberg, D. Alignment of Boron Nitride Nanotubes in Polymeric Composite Films for Thermal Conductivity Improvement. *J. Phys. Chem. C* **2010**, *114* (10), 4340–4344. https://doi.org/10.1021/jp911431f.

(10) Yamaguchi, M.; Pakdel, A.; Zhi, C.; Bando, Y.; Tang, D.-M.; Faerstein, K.; Shtansky, D.; Golberg, D. Utilization of Multiwalled Boron Nitride Nanotubes for the Reinforcement of Lightweight Aluminum Ribbons. *Nanoscale Res. Lett.* **2013**, *8* (1), 3. https://doi.org/10.1186/1556-276X-8-3.

(11) Xue, Y.; Jiang, B.; Bourgeois, L.; Dai, P.; Mitome, M.; Zhang, C.; Yamaguchi, M.; Matveev, A.; Tang, C.; Bando, Y.; et al. Aluminum Matrix Composites Reinforced with Multi-Walled Boron Nitride Nanotubes Fabricated by a High-Pressure Torsion Technique. *Mater. Des.* **2015**, *88*, 451–460. https://doi.org/10.1016/j.matdes.2015.08.162.

(12) Nautiyal, P.; Rudolf, C.; Loganathan, A.; Zhang, C.; Boesl, B.; Agarwal, A. Directionally Aligned Ultra-Long Boron Nitride Nanotube Induced Strengthening of Aluminum-Based Sandwich Composite: Boron Nitride Nanotube Induced Strengthening of Aluminum Composite. *Adv. Eng. Mater.* **2016**, *18* (10), 1747–1754. https://doi.org/10.1002/adem.201600212.

(13) Tiano, A. L.; Gibbons, L.; Tsui, M.; Applin, S. I.; Silva, R.; Park, C.; Fay, C. C. Thermodynamic Approach to Boron Nitride Nanotube Solubility and Dispersion. *Nanoscale* **2016**, *8* (7), 4348–4359. https://doi.org/10.1039/C5NR08259E.

(14) Thibeault, S. A.; Kang, J. H.; Sauti, G.; Park, C.; Fay, C. C.; King, G. C. Nanomaterials for Radiation Shielding. *MRS Bull.* **2015**, *40* (10), 836–841. https://doi.org/10.1557/mrs.2015.225.

(15) Li, Y.; Zhou, Z.; Golberg, D.; Bando, Y.; Schleyer, P. von R.; Chen, Z. Stone–Wales Defects in Single-Walled Boron Nitride Nanotubes: Formation Energies, Electronic Structures, and Reactivity. *J. Phys. Chem. C* **2008**, *112* (5), 1365–1370. https://doi.org/10.1021/jp077115a.

(16) Radosavljević, M.; Appenzeller, J.; Derycke, V.; Martel, R.; Avouris, P.; Loiseau, A.; Cochon, J.-L.; Pigache, D. Electrical Properties and Transport in Boron Nitride Nanotubes. *Appl. Phys. Lett.* **2003**, *82* (23), 4131–4133. https://doi.org/10.1063/1.1581370.

(17) El Khalifi, M.; Bentin, J.; Duverger, E.; Gharbi, T.; Boulahdour, H.; Picaud, F. Encapsulation Capacity and Natural Payload Delivery of an Anticancer Drug from Boron Nitride Nanotube. *Phys. Chem. Chem. Phys.* **2016**, *18* (36), 24994–25001. https://doi.org/10.1039/C6CP01387B.

(18) Yu, J.; Chen, Y.; Cheng, B. M. Dispersion of Boron Nitride Nanotubes in Aqueous Solution with the Help of Ionic Surfactants. *Solid State Commun.* **2009**, *149* (19–20), 763–766. https://doi.org/10.1016/j.ssc.2009.03.001.

(19) Golberg, D.; Bando, Y.; Huang, Y.; Terao, T.; Mitome, M.; Tang, C.; Zhi, C. Boron Nitride Nanotubes and Nanosheets. *ACS Nano* **2010**, *4* (6), 2979–2993. https://doi.org/10.1021/nn1006495.

(20) Lourie, O. R.; Jones, C. R.; Bartlett, B. M.; Gibbons, P. C.; Ruoff, R. S.; Buhro, W. E. CVD Growth of Boron Nitride Nanotubes. *Chem. Mater.* **2000**, *12* (7), 1808–1810. https://doi.org/10.1021/cm000157q.

(21) Lee, C. H.; Wang, J.; Kayatsha, V. K.; Huang, J. Y.; Yap, Y. K. Effective Growth of Boron Nitride Nanotubes by Thermal Chemical Vapor Deposition. *Nanotechnology* **2008**, *19* (45), 455605. https://doi.org/10.1088/0957-4484/19/45/455605.

(22) Lee, C. H.; Xie, M.; Kayastha, V.; Wang, J.; Yap, Y. K. Patterned Growth of Boron Nitride Nanotubes by Catalytic Chemical Vapor Deposition. *Chem. Mater.* **2010**, *22* (5), 1782–1787. https://doi.org/10.1021/cm903287u.

(23) Wang, J.; Kayastha, V. K.; Yap, Y. K.; Fan, Z.; Lu, J. G.; Pan, Z.; Ivanov, I. N.; Puretzky, A. A.; Geohegan, D. B. Low Temperature Growth of Boron Nitride Nanotubes on Substrates. *Nano Lett.* **2005**, *5* (12), 2528–2532. https://doi.org/10.1021/nl051859n.

(24) Huang, Y.; Lin, J.; Tang, C.; Bando, Y.; Zhi, C.; Zhai, T.; Dierre, B.; Sekiguchi, T.; Golberg, D. Bulk Synthesis, Growth Mechanism and Properties of Highly Pure Ultrafine Boron Nitride Nanotubes with Diameters of Sub-10 Nm. *Nanotechnology* **2011**, *22* (14), 145602. https://doi.org/10.1088/0957-4484/22/14/145602.

(25) Han, W.; Bando, Y.; Kurashima, K.; Sato, T. Synthesis of Boron Nitride Nanotubes from Carbon Nanotubes by a Substitution Reaction. *Appl. Phys. Lett.* **1998**, *73* (21), 3085–3087. https://doi.org/10.1063/1.122680.

(26) Bechelany, M.; Bernard, S.; Brioude, A.; Cornu, D.; Stadelmann, P.; Charcosset, C.; Fiaty, K.; Miele, P. Synthesis of Boron Nitride Nanotubes by a Template-Assisted Polymer Thermolysis Process. *J. Phys. Chem. C* **2007**, *111* (36), 13378–13384. https://doi.org/10.1021/jp074178k.

(27) Smith, M. W.; Jordan, K. C.; Park, C.; Kim, J.-W.; Lillehei, P. T.; Crooks, R.; Harrison, J. S. Very Long Single- and Few-Walled Boron Nitride Nanotubes via the Pressurized Vapor/Condenser Method. *Nanotechnology* **2009**, *20* (50), 505604. https://doi.org/10.1088/0957-4484/20/50/505604.

(28) Kim, K. S.; Kingston, C. T.; Hrdina, A.; Jakubinek, M. B.; Guan, J.; Plunkett, M.; Simard, B. Hydrogen-Catalyzed, Pilot-Scale Production of Small-Diameter Boron Nitride Nanotubes and Their Macroscopic Assemblies. *ACS Nano* **2014**, *8* (6), 6211–6220. https://doi.org/10.1021/nn501661p.

(29) Fathalizadeh, A.; Pham, T.; Mickelson, W.; Zettl, A. Scaled Synthesis of Boron Nitride Nanotubes, Nanoribbons, and Nanococoons Using Direct Feedstock Injection into an Extended-Pressure, Inductively-Coupled Thermal Plasma. *Nano Lett.* **2014**, *14* (8), 4881–4886. https://doi.org/10.1021/nl5022915.

(30) Liao, Y.; Chen, Z.; Connell, J. W.; Fay, C. C.; Park, C.; Kim, J.-W.; Lin, Y. Chemical Sharpening, Shortening, and Unzipping of Boron Nitride Nanotubes. *Adv. Funct. Mater.* **2014**, *24* (28), 4497–4506. https://doi.org/10.1002/adfm.201400599.

(31) Jakubinek, M. B.; Niven, J. F.; Johnson, M. B.; Ashrafi, B.; Kim, K. S.; Simard, B.; White, M. A. Thermal Conductivity of Bulk Boron Nitride Nanotube Sheets and Their Epoxy-Impregnated Composites: Thermal Conductivity of Bulk Boron Nitride Nanotube Sheets. *Phys. Status Solidi A* **2016**, *213* (8), 2237–2242. https://doi.org/10.1002/pssa.201533010.

(32) Zhi, C.; Bando, Y.; Terao, T.; Tang, C.; Kuwahara, H.; Golberg, D. Towards Thermoconductive, Electrically Insulating Polymeric Composites with Boron Nitride Nanotubes as Fillers. *Adv. Funct. Mater.* **2009**, *19* (12), 1857–1862. https://doi.org/10.1002/adfm.200801435.

(33) Behabtu, N.; Young, C. C.; Tsentalovich, D. E.; Kleinerman, O.; Wang, X.; Ma, A. W. K.; Bengio, E. A.; ter Waarbeek, R. F.; de Jong, J. J.; Hoogerwerf, R. E.; et al. Strong, Light, Multifunctional Fibers of Carbon Nanotubes with Ultrahigh Conductivity. *Science* **2013**, *339* (6116), 182–186. https://doi.org/10.1126/science.1228061.

(34) Chen, H.; Chen, Y.; Yu, J.; Williams, J. S. Purification of Boron Nitride Nanotubes. *Chem. Phys. Lett.* **2006**, *425* (4–6), 315–319. https://doi.org/10.1016/j.cplett.2006.05.058.

(35) Zhi, C.; Bando, Y.; Tang, C.; Xie, R.; Sekiguchi, T.; Golberg, D. Perfectly Dissolved Boron Nitride Nanotubes Due to Polymer Wrapping. *J. Am. Chem. Soc.* **2005**, *127* (46), 15996–15997. https://doi.org/10.1021/ja053917c.

(36) Xie, S.-Y.; Wang, W.; Fernando, K. A. S.; Wang, X.; Lin, Y.; Sun, Y.-P. Solubilization of Boron Nitride Nanotubes. *Chem. Commun.* **2005**, *0* (29), 3670. https://doi.org/10.1039/b505330g.

(37) Velayudham, S.; Lee, C. H.; Xie, M.; Blair, D.; Bauman, N.; Yap, Y. K.; Green, S. A.; Liu, H. Noncovalent Functionalization of Boron Nitride Nanotubes with Poly(*p* -Phenylene-Ethynylene)s and Polythiophene. *ACS Appl. Mater. Interfaces* **2010**, *2* (1), 104–110. https://doi.org/10.1021/am900613j.

(38) Zhi, C.; Bando, Y.; Tang, C.; Honda, S.; Sato, K.; Kuwahara, H.; Golberg, D. Purification of Boron Nitride Nanotubes through Polymer Wrapping. *J. Phys. Chem. B* **2006**, *110* (4), 1525–1528. https://doi.org/10.1021/jp054941f.

(39) Ansari, R.; Ajori, S.; Ameri, A. Stability Characteristics and Structural Properties of Single- and Double-Walled Boron-Nitride Nanotubes under Physical Adsorption of Flavin Mononucleotide (FMN) in Aqueous Environment Using Molecular Dynamics Simulations. *Appl. Surf. Sci.* **2016**, *366*, 233–244. https://doi.org/10.1016/j.apsusc.2016.01.098.

(40) Lee, C. H.; Zhang, D.; Yap, Y. K. Functionalization, Dispersion, and Cutting of Boron Nitride Nanotubes in Water. *J. Phys. Chem. C* **2012**, *116* (2), 1798–1804. https://doi.org/10.1021/jp2112999.

(41) Adnan, M.; Marincel, D. M.; Kleinerman, O.; Chu, S.-H.; Park, C.; Hocker, S. J. A.; Fay, C.; Arepalli, S.; Talmon, Y.; Pasquali, M. Extraction of Boron Nitride Nanotubes and Fabrication of Macroscopic Articles Using Chlorosulfonic Acid. *Nano Lett.* **2018**, *18* (3), 1615–1619. https://doi.org/10.1021/acs.nanolett.7b04335.

(42) Lucas, A.; Zakri, C.; Maugey, M.; Pasquali, M.; van der Schoot, P.; Poulin, P. Kinetics of Nanotube and Microfiber Scission under Sonication. *J. Phys. Chem. C* **2009**, *113* (48), 20599–20605. https://doi.org/10.1021/jp906296y.

(43) Jacobson, N.; Farmer, S.; Moore, A.; Sayir, H. High-Temperature Oxidation of Boron Nitride: I, Monolithic Boron Nitride. *J. Am. Ceram. Soc.* **1999**, *82* (2), 393–398. https://doi.org/10.1111/j.1551-2916.1999.tb20075.x.

(44) Chen, Y. K.; Liu, L. V.; Wang, Y. A. Density Functional Study of Interaction of Atomic Pt with Pristine and Stone–Wales-Defective Single-Walled Boron Nitride Nanotubes. *J. Phys. Chem. C* **2010**, *114* (29), 12382–12388. https://doi.org/10.1021/jp9078508.

(45) An, W.; Wu, X.; Yang, J. L.; Zeng, X. C. Adsorption and Surface Reactivity on Single-Walled Boron Nitride Nanotubes Containing Stone–Wales Defects. *J. Phys. Chem. C* **2007**, *111* (38), 14105–14112. https://doi.org/10.1021/jp072443w.

(46) Sainsbury, T.; Satti, A.; May, P.; Wang, Z.; McGovern, I.; Gun'ko, Y. K.; Coleman, J. Oxygen Radical Functionalization of Boron Nitride Nanosheets. *J. Am. Chem. Soc.* **2012**, *134* (45), 18758–18771. https://doi.org/10.1021/ja3080665.

(47) Zhao, J.; Ding, Y. Theoretical Investigation of the Divacancies in Boron Nitride Nanotubes: Properties and Surface Reactivity toward Various Adsorbates. *J. Chem. Phys.* **2009**, *131* (1), 014706. https://doi.org/10.1063/1.3167409.

(48) Costa Paura, E. N.; da Cunha, W. F.; Roncaratti, L. F.; Martins, J. B. L.; e Silva, G. M.; Gargano, R. CO ₂ Adsorption on Single-Walled Boron Nitride Nanotubes Containing Vacancy Defects. *RSC Adv.* **2015**, *5* (35), 27412–27420. https://doi.org/10.1039/C4RA17336H.

(49) Okada, S. Atomic Configurations and Energetics of Vacancies in Hexagonal Boron Nitride: First-Principles Total-Energy Calculations. *Phys. Rev. B* **2009**, *80* (16). https://doi.org/10.1103/PhysRevB.80.161404.

(50) Azevedo, S.; Kaschny, J. R.; de Castilho, C. M. C.; de Brito Mota, F. A Theoretical Investigation of Defects in a Boron Nitride Monolayer. *Nanotechnology* **2007**, *18* (49), 495707. https://doi.org/10.1088/0957-4484/18/49/495707.

(51) Petravic, M.; Peter, R.; Kavre, I.; Li, L. H.; Chen, Y.; Fan, L.-J.; Yang, Y.-W. Decoration of Nitrogen Vacancies by Oxygen Atoms in Boron Nitride Nanotubes. *Phys. Chem. Chem. Phys.* **2010**, *12* (47), 15349. https://doi.org/10.1039/c0cp00984a.

(52) Zhao, J.; Ding, Y. Theoretical Studies of the Interaction of an Open-Ended Boron Nitride Nanotube (BNNT) with Gas Molecules. *J. Phys. Chem. C* **2008**, *112* (51), 20206–20211. https://doi.org/10.1021/jp805790s.

(53) Lin, Y.; Williams, T. V.; Cao, W.; Elsayed-Ali, H. E.; Connell, J. W. Defect Functionalization of Hexagonal Boron Nitride Nanosheets. *J. Phys. Chem. C* **2010**, *114* (41), 17434–17439. https://doi.org/10.1021/jp105454w.

(54) Auwärter, W.; Muntwiler, M.; Osterwalder, J.; Greber, T. Defect Lines and Two-Domain Structure of Hexagonal Boron Nitride Films on Ni(111). *Surf. Sci.* **2003**, *545* (1–2), L735–L740. https://doi.org/10.1016/j.susc.2003.08.046.

(55) Deng, Z.-Y.; Zhang, J.-M. First-Principles Study of O_2 and Cl_2 Molecule Adsorption on Pristine Doped Boron Nitride Nanotubes. *Can. J. Phys.* **2016**, *94* (10), 1071–1079. https://doi.org/10.1139/cjp-2016-0326.

(56) *Handbook of X-Ray Photoelectron Spectroscopy: A Reference Book of Standard Spectra for Identification and Interpretation of XPS Data*; Moulder, J. F., Stickle, W. F., Sobol, P. E., Bomben, K. D., Chastain, J., King Jr., R. C., Physical Electronics, Incorporation, Eds.; Physical Electronics: Eden Prairie, Minn., 1995.

(57) Powell, C. X-Ray Photoelectron Spectroscopy Database XPS,Version 4.1, NIST Standard Reference Database 20, 1989. https://doi.org/10.18434/T4T88K.

(58) Wahbeh, B.; Hamed, T. A.; Kasher, R. Hydrogen and Boric Acid Production via Boron Hydrolysis. *Renew. Energy* **2012**, *48*, 10–15. https://doi.org/10.1016/j.renene.2012.04.043.

(59) Rohani, P.; Kim, S.; Swihart, M. T. Boron Nanoparticles for Room-Temperature Hydrogen Generation from Water. *Adv. Energy Mater.* **2016**, *6* (12), 1502550. https://doi.org/10.1002/aenm.201502550.

(60) Kracek, F. C.; Morey, G. W.; Merwin, H. E. The System, Water-Boron Oxide. *Am J Sci A* **1938**, *35*, 143–171.

(61) Streletskii, A. N.; Permenov, D. G.; Bokhonov, B. B.; Leonov, A. V.; Mudretsova, S. N. Mechanochemistry of Hexagonal Boron Nitride. 2. Reactivity upon Interaction with Water. *Colloid J.* **2010**, *72* (4), 553–558. https://doi.org/10.1134/S1061933X10040174.

(62) Yao, N.; Lordi, V.; Ma, S. X. C.; Dujardin, E.; Krishnan, A.; Treacy, M. M. J.; Ebbesen, T. W. Structure and Oxidation Patterns of Carbon Nanotubes. *J. Mater. Res.* **1998**, *13* (09), 2432–2437. https://doi.org/10.1557/JMR.1998.0338.

(63) Hernadi, K.; Siska, A.; Thiên-Nga, L.; Forró, L.; Kiricsi, I. Reactivity of Different Kinds of Carbon during Oxidative Purification of Catalytically Prepared Carbon Nanotubes. *Solid State Ion.* **2001**, *141–142*, 203–209. https://doi.org/10.1016/S0167-2738(01)00789-5.

(64) Zimmerman, J. L.; Bradley, R. K.; Huffman, C. B.; Hauge, R. H.; Margrave, J. L. Gas-Phase Purification of Single-Wall Carbon Nanotubes. *Chem. Mater.* **2000**, *12* (5), 1361–1366. https://doi.org/10.1021/cm990693m.

(65) Hendrickson, D. N.; Hollander, J. M.; Jolly, W. L. Core-Electron Binding Energies for Compounds of Boron, Carbon, and Chromium. *Inorg. Chem.* **1970**, *9* (3), 612–615. https://doi.org/10.1021/ic50085a035.

(66) Belyansky, M.; Trenary, M.; Ellison, C. Boron Chemical Shifts in B6O. *Surf. Sci. Spectra* **1994**, *3* (2), 147–150. https://doi.org/10.1116/1.1247776.

(67) Shul-Ga, Y. M.; Moravskaya, T. M.; Gurov, S. V.; Chukalin, V. I.; Borod'ko, Y. G. XPS and ELS Study of Boron Nitride Ultrafine Powder. *Phys Chem Mech Surf* **1991**, *6* (10), 2618–2622.

(68) Gouin, X.; Grange, P.; Bois, L.; L'Haridon, P.; Laurent, Y. Characterization of the Nitridation Process of Boric Acid. *J. Alloys Compd.* **1995**, *224* (1), 22–28. https://doi.org/10.1016/0925-8388(95)01532-9.

(69) Burke, A. R.; Brown, C. R.; Bowling, W. C.; Glaub, J. E.; Kapsch, D.; Love, C. M.; Whitaker, R. B.; Moddeman, W. E. Ignition Mechanism of the Titanium-Boron Pyrotechnic Mixture. *Surf. Interface Anal.* **1988**, *11* (6–7), 353–358. https://doi.org/10.1002/sia.740110614.

(70) Herrmann, M.; Thiele, M.; Jaenicke-Roessler, K.; Freemantle, C. S.; Sigalas, I. Oxidation Resistance of B6O-Materials with Different Additives. *J. Eur. Ceram. Soc.* **2011**, *31* (9), 1771–1777. https://doi.org/10.1016/j.jeurceramsoc.2011.03.029.

(71) Jain, A.; Joseph, K.; Anthonysamy, S.; Gupta, G. S. Kinetics of Oxidation of Boron Powder. *Thermochim. Acta* **2011**, *514* (1–2), 67–73. https://doi.org/10.1016/j.tca.2010.12.004.

(72) Jain, A.; Anthonysamy, S.; Ananthasivan, K.; Gupta, G. S. Studies on the Ignition Behaviour of Boron Powder. *Thermochim. Acta* **2010**, *500* (1–2), 63–68. https://doi.org/10.1016/j.tca.2009.12.011.

(73) Geick, R.; Perry, C. H.; Rupprecht, G. Normal Modes in Hexagonal Boron Nitride. *Phys. Rev.* **1966**, *146* (2), 543–547. https://doi.org/10.1103/PhysRev.146.543.

(74) Wirtz, L.; Rubio, A. Vibrational Properties of Boron-Nitride Nanotubes: Effects of Finite Length and Bundling. *IEEE Trans. Nanotechnol.* **2003**, *2* (4), 341–348. https://doi.org/10.1109/TNANO.2003.820511.

(75) Ohba, N.; Miwa, K.; Nagasako, N.; Fukumoto, A. First-Principles Study on Structural, Dielectric, and Dynamical Properties for Three BN Polytypes. *Phys. Rev. B* **2001**, *63* (11). https://doi.org/10.1103/PhysRevB.63.115207.

(76) Michel, K. H.; Verberck, B. Phonon Dispersions and Piezoelectricity in Bulk and Multilayers of Hexagonal Boron Nitride. *Phys. Rev. B* **2011**, *83* (11). https://doi.org/10.1103/PhysRevB.83.115328.

(77) Hubáček, M.; Sato, T.; Ishii, T. A Coexistence of Boron Nitride and Boric Oxide. *J. Solid State Chem.* **1994**, *109* (2), 384–390. https://doi.org/10.1006/jssc.1994.1117.

(78) Kleinerman, O.; Parra-Vasquez, A. N. G.; Green, M. J.; Behabtu, N.; Schmidt, J.; Kesselman, E.; Young, C. C.; Cohen, Y.; Pasquali, M.; Talmon, Y. Cryogenic-Temperature Electron Microscopy Direct Imaging of Carbon Nanotubes and Graphene Solutions in Superacids. *J. Microsc.* **2015**, *259* (1), 16–25. https://doi.org/10.1111/jmi.12243.

(79) Green, M. J.; Young, C. C.; Parra-Vasquez, A. N. G.; Majumder, M.; Juloori, V.; Behabtu, N.; Pint, C. L.; Schmidt, J.; Kesselman, E.; Hauge, R. H.; et al. Direct Imaging of Carbon Nanotubes Spontaneously Filled with Solvent. *Chem Commun* **2011**, *47* (4), 1228–1230. https://doi.org/10.1039/C0CC03915B.

(80) Kleinerman, O.; Adnan, M.; Marincel, D. M.; Ma, A. W. K.; Bengio, E. A.; Park, C.; Chu, S.-H.; Pasquali, M.; Talmon, Y. Dissolution and Characterization of Boron Nitride Nanotubes in Superacid. *Langmuir* **2017**, *33* (50), 14340–14346. https://doi.org/10.1021/acs.langmuir.7b03461.

SYNOPSIS TOC